Received: 8 September 2023 | Revised: 14 November 2023 | Accepted: 21 November 2023 | Published online: 1 December 2023

RESEARCH ARTICLE

Journal of Computational and Cognitive Engineering
2024, Vol. 3(1) 15–23
DOI: 10.47852/bonviewJCCE32021698

BON VIEW PUBLISHING

# Investigating and Classifying the Level of Thermal Runaway-Induced Failure Energy Storage Systems in Photovoltaics

**Nikta Shamsmohammadi**[1,*]

[1]*Department of Information and Electrical Engineering and Applied Mathematics, University of Salerno, Italy*

**Abstract:** In a photovoltaic system, the electricity generated by a solar panel can depend on the amount of sunlight available at any given time. Due to the nonlinear behavior of this energy, the storage component of the system is critical. As a result, many solar panel systems are equipped with batteries. However, changes in environmental and other conditions can cause damage to these batteries. This study explores novel technologies for detecting thermal runaway failures in lithium-ion batteries. Specifically, the study employs image processing techniques to detect structural failures and applies deep learning techniques for automatic classification. Thermal damage to a battery can result in irreparable harm, making design and construction considerations crucial. Through image analysis, any internal changes in the battery can be transformed into a measurable variable, providing a reliable indication of potential failure. The study compares the current series with previous ones to highlight the structural differences. Results confirm that the proposed approach has significant potential for detecting and estimating internal variations during production. Overall, the proposed method can serve as a valuable tool for drafting and implementing a comprehensive plan to address early problems in the battery.

**Keywords:** failure analysis, thermal image, image processing, convolutional neural network (CNN) classification, transfer learning

## 1. Introduction

In today's world, the harvesting of energy from the environment has become a significant research and industrial operation due to its crucial importance (Rahimzadeh et al., 2021). Energy can be harvested from various sources, ranging from small-scale environmental vibration (Rahimzadeh et al., 2023) for use in transportation systems (Guido et al., 2022) or in large-scale from solar energy for agrivoltaics applications (Mouhib et al., 2022). Among these, solar panels, also known as photovoltaic (PV) panels, are capable of generating electricity by converting sunlight energy into electrical energy. However, the amount of electricity generated by a solar panel is subject to variation, depending on the availability of sunlight at any given time. Due to the nonlinear nature of this energy (Samadi et al., 2022), many solar panel systems are equipped with batteries that ensure a stable supply of electricity (Abbott & Cohen, 2020). These batteries store the excess electricity produced by the solar panels during periods of high sunlight intensity, which can be used later when the demand for electricity exceeds the amount produced by the solar panels (Richardson & Harvey, 2015), when the system is disrupted, or when access to electricity is limited. This mechanism helps to ensure a constant supply of electricity, irrespective of the level of sunlight at any given time (Nabil & Mardaljevic, 2006). When it comes to selecting a battery for a solar panel system (Khatib et al., 2016), there are various factors that need to be considered. These include the size and type of the solar panel system, the amount of energy required by the system, and the environmental conditions in which the system will operate. It is important to note that the system may be exposed to harsh weather conditions, which could potentially damage or even destroy the battery, leading to a loss of energy from the solar panel system (Boxwell, 2010). Therefore, it is crucial to take into account the environmental conditions of the installation location when selecting a battery. The battery should be chosen based on its ability to withstand the specific environmental conditions of the installation location and provide reliable performance throughout its expected lifetime (Dehghani-Sanij et al., 2019). Thermal runaway can potentially occur in various types of batteries, but it is more commonly associated with certain battery chemicals due to their specific characteristics. The most notable battery types that are susceptible to thermal runaway are lithium-polymer batteries, lithium-ion phosphate (LiFePO4) batteries, lithium cobalt oxide (LiCoO2) batteries, lithium iron phosphate (LiFePO4) batteries, lead-acid batteries, lithium-ion batteries, etc. (Kim et al., 2020). Lithium-ion batteries are known for their high-energy density but can be prone to thermal runaway if subjected to overcharging, over discharge, physical damage, or exposure to high temperatures. Compared to other high-energy density batteries, Kamali-Heidari et al. (2018) noted that lithium-ion batteries are a relatively new technology that offers several advantages, including lightweight, low maintenance, and a longer lifespan. However, it is crucial to consider temperature as a critical factor in the design of solar panel systems that use lithium-ion batteries (Amelia et al., 2016). Extreme heat or cold can significantly impact the performance of these batteries, and the thermal band level of lithium-ion batteries used in PV panels can

*Corresponding author: Nikta Shamsmohammadi, Department of Information and Electrical Engineering and Applied Mathematics, University of Salerno, Italy. Email: nshamsmohammadi@unisa.it

vary based on various factors, such as the type and quality of the battery, the operating conditions of the PV panel system, and the specific safety mechanisms that are in place. The most notable battery types that are susceptible to thermal runaway are lithium-polymer batteries, lithium-ion phosphate (LiFePO4) batteries, lithium cobalt oxide (LiCoO2) batteries, lithium iron phosphate (LiFePO4) batteries, lead-acid batteries, lithium-ion batteries, etc. (Xu et al., 2021). Therefore, it is essential to thoroughly assess these factors to ensure that the lithium-ion battery is optimally utilized and can deliver consistent and reliable performance throughout its lifetime.

Thermal runaway can potentially occur in various types of batteries, but it is more commonly associated with certain battery chemicals due to their specific characteristics. Lithium-ion batteries are widely used in portable electronics, electric vehicles, and energy storage systems. Thermal runaway is a serious concern for lithium-ion batteries used in PV panel systems (Golubkov et al., 2014). Such batteries can experience thermal runaway due to exposure to high temperatures, mechanical damage, or internal component failure. Overcharging a battery can cause excessive heat generation and potentially lead to thermal runaway. If a battery is continually charged beyond its recommended voltage or current limits, it can become unstable. Also, discharging a battery beyond its specified lower voltage limit can lead to thermal runaway. This can occur when a battery is drained to the point where it reverses its chemical reactions, releasing heat in the process (Finegan et al., 2017). When thermal runaway occurs, the heat generated by the battery's chemical reactions causes further breakdown of the electrolyte and electrodes, leading to the release of flammable gases such as hydrogen and carbon monoxide. As the heat and gas production continue to increase, the battery becomes increasingly unstable, and the pressure inside the battery can rise rapidly. If the pressure becomes too high, the battery can rupture or explode, resulting in potential fires or the release of toxic gases (Tran et al., 2022). Once thermal runaway has begun, it is challenging to stop, and it can spread to other cells in a battery pack, making it a severe safety hazard. To prevent thermal runaway in a PV panel system, it is vital to follow proper safety protocols during battery production and testing (Chen et al., 2021) and to have accurate information about the battery's tolerance levels, such as monitoring the battery's temperature and voltage and designing an appropriate storage system. By controlling such factors, it is possible to prevent damage from occurring in the battery and avoid costly repairs or replacements. Investigating such cases can be achieved through the utilization of image processing techniques. Furthermore, the identification of battery failure is a crucial technical task that demands the utmost precision and accuracy. Given the importance of this issue, this article used histogram analysis and Fourier transform (FT) image analysis to investigate and identify battery damage from thermal runaway video (Afifah et al., 2020; Jung et al., 2019; Tsai et al., 2012). Then, using the convolutional neural network (CNN) method (Wang et al., 2017), the failure rate was categorized into four stages. These methods can be used to analyze the distribution of the battery's lifecycle, identify any performance trends or patterns, and compare the performance of different battery designs or manufacturing processes.

## 2. Research Methodology

### 2.1. Dataset

The 18650 battery is a popular type of lithium-ion rechargeable battery known for its high-energy density and versatile applications and portable devices but requires careful handling to ensure safety.

**Table 1**
**Specifications of models of 18650 batteries**

| Model | Capacity (Ah) | Voltage (V) | Wall thickness | Bottom vent |
|---|---|---|---|---|
| Storia 18650 | 2.1 Ah | 4.2 V | 250 μm | No |
| KULR 18650-K330 | 3.3 Ah | 4.2 V | 220 μm | Yes |
| LG 18650-M36 | 3.4 Ah | 4.2 V | 250 μm | No |
| MOLiCEL 18650-j | 2.3 Ah | 4.2 V | 203 μm | No |

Table 1 shows the specifications of four models of 18650 batteries, and in this study, the Soteria 18650 model was investigated through high-speed radiography during thermal runaway.

The radiography video that we analyzed depicts a Soteria Li-ion 18650 cell in a 100% state of charge undergoing thermal abuse inside a fractional thermal runaway calorimeter. The radiography was recorded at a rate of 2000 frames per second at the European Synchrotron Radiation Facility. The location of the field of view longitudinally was top of the battery which the image consisted of 2016 × 1111 pixels with a pixel size of 10 μm (Keyser et al., 2015; National Renewable Energy Laboratory, 2020).

In the context of video processing, a frame refers to a static image from a collection of images that constitute a video. Essentially, a video is a sequence of frames that are displayed rapidly in succession. Each frame in a video contains information about the position, color, and intensity of every pixel in the image. The resolution of a video frame is determined by its width and height in pixels, and frames can be examined and processed individually or in sequence to extract information about motion, object detection, and other features.

Figure 1 shows the process of battery damage under the effect of thermal runaway.

In this article, we extracted 1192 continuous images from 64 s of high-speed X-ray radiography videos of lithium-ion batteries. These images were compared at intervals of every 0.001 s to observe the behavior of the battery during the test. For example, an image can be compared to its preceding or succeeding image at

**Figure 1**
**The different stages of the battery's behavior: (a) Stage 1: The battery is in good working condition, (b) Stage 2: Involves a minor shift of the electrode assembly toward the vent, (c) Stage 3: Involves the stretching of the spin groove due to the force applied by the electrode assembly on the crimp components, and (d) Stage 4: Ejection of the electrode assembly, completing the bursting process**

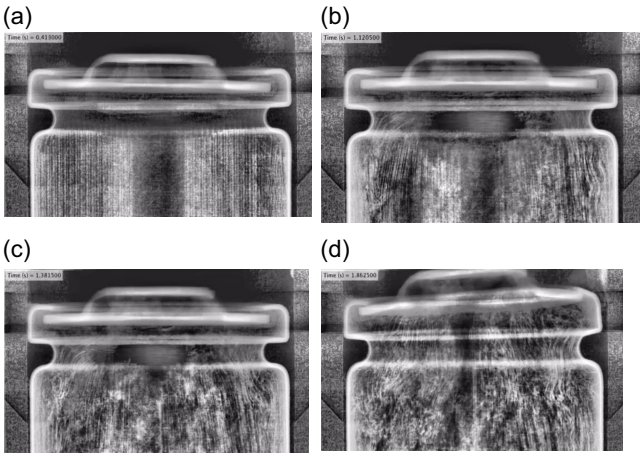

**Table 2**
**Stage-level quantities**

| Stage level | Image label | Image quantity |
|---|---|---|
| Stage 1 | 1 | 206 |
| Stage 2 | 2 | 540 |
| Stage 3 | 3 | 325 |
| Stage 4 | 4 | 121 |
| **Total** | | **1192** |

various time intervals, or a particular image can be compared to a sequence of other images. Although changes that occur over time in batteries may not be perceptible to the naked eye, it is exceedingly difficult to determine the precise location where the change began or the exact point at which it initiated in the early stages. The analyses from this pilot study furnish valuable information to guide future research and establish initial definitions for the four stages. The size of the input images is (224, 224, 3) for grayscale images and the numbers of images available for each stage are detailed in Table 2. Since the number of images varied for each failure stage, it was essential to partition the stage-level classes based on these proportions.

Consequently, the data for each of the three divided datasets (train, validation, and test) were stored in separate files, each associated with a specific path and label.

## 2.2. Monitoring and diagnosis methods

Generally, various methods are employed to analyze and diagnose system failures. For example, one method is to use thresholding and check binary images. Various features can be extracted from the binary image that are indicative of the failure, like area, perimeter, shape factors, etc. These features can then be used as inputs for a classifier. Also, one of the best ways to find the right threshold for an image is to check its histogram. This involves constructing a histogram of the relevant data and analyzing the distribution of values to identify any patterns or abnormalities that may indicate a failure.

A histogram is a chart frequently utilized in data analysis for depicting the distribution of values within a dataset and for identifying patterns in the data. To improve the visual clarity of images, an equalization process is often applied. This process involves redistributing the most common intensities with a nearly linear cumulative distribution, which allows for a certain level of tolerance intensity values when comparing consecutive images. The formula for histogram equalization is typically expressed in a general form as follows:

$$T(k) = \left[\frac{cdf(k) - cdf_m}{N - cdf_m}\right] \quad (1)$$

The formula for histogram equalization involves the output value of input intensity $k$ after undergoing grayscale transformation $T$, denoted by $T(k)$. The cumulative distribution function value of input intensity $k$ is represented by $cdf(k)$, while $cdf_m$ denotes the minimum non-zero value of the cumulative distribution function. $N$ represents the total number of pixels in the image matrix.

In the realm of Li-ion batteries, a histogram analysis can be employed to investigate the distribution of key performance

**Figure 2**
**(a) Histogram of stage 1, (b) Histogram of stage 4, and (c) Comparison of the histogram of stage 1 and stage (a)**

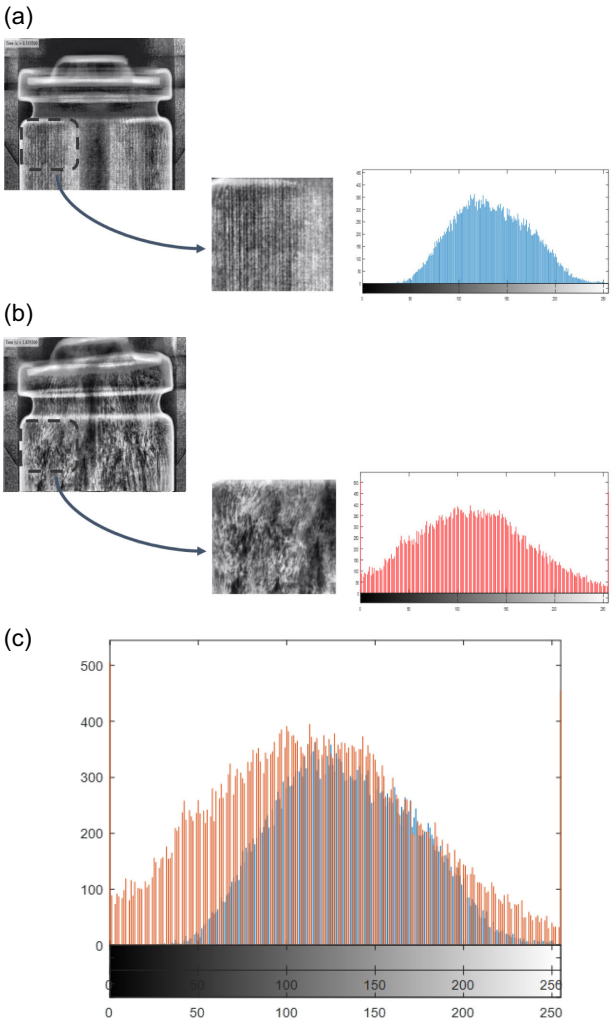


metrics, such as capacity, energy density, or cycle life, throughout a population of batteries. This technique can be utilized to identify any patterns or trends in the data, as well as to detect any outliers or anomalous behavior that may indicate defects or other issues with the batteries. In Figure 2, we examined the histogram of a part of the internal texture of the stage 1 and stage 4 battery images

As demonstrated in Figure 2, the histogram analysis of two images showed considerable disparities when comparing normal values to error values. By examining the histogram pattern of a healthy battery, it is feasible to detect any abnormalities in a damaged battery by comparing the two histograms. The histogram of a healthy battery is typically characterized by a nearly symmetrical distribution of values, whereas a defective battery's histogram is often asymmetrical or skewed. Also, the histogram pattern of a healthy battery can exhibit variability depending on the performance metric being analyzed, such as capacity, energy density, or cycle life. Conversely, a damaged battery's histogram pattern will typically feature a wider and more varied distribution of values, as depicted in the image of the defective battery.

By comparing the histogram patterns of healthy and damaged batteries, it is possible to detect any abnormalities or issues that may require further investigation or correction. Also, another suitable way to analyze is the FT of the image. Unique frequencies present in different failure types can act as features for classification. This transformation enables the analysis and interpretation of frequency components present in the image, including edges, textures, and patterns that may not be easily discernible in the spatial domain. The discrete Fourier transform (DFT) of an image is computed by taking the 2D FT of each pixel in the image, resulting in a matrix.

Suppose $f(x, y)$ represents the gray level at pixel coordinates $(x, y)$ in an image of size $M \times N$. The two-dimensional DFT of $f(x, y)$ can be expressed as follows:

$$F(u,v) = \sum_{y=0}^{N-1} \sum_{x=0}^{M-1} f(x,y).\, exp\left[-j2\pi\left(\frac{ux}{M} + \frac{vy}{N}\right)\right] \tag{2}$$

For spectral variables $u = 0, 1, 2, \ldots, M-1$ and $v = 0, 1, 2, \ldots, N-1$. The DFT is typically complex, that is:

$$F(u,v) = R(u,v) + j.I(u,v) \tag{3}$$

where $R(u, v)$ and $I(u, v)$ are the real and imaginary parts of $F(u, v)$, i.e.,

$$R(u,v) = \sum_{y=0}^{N-1} \sum_{x=0}^{M-1} f(x,y).\, \cos\left[2\pi\left(\frac{ux}{M} + \frac{vy}{N}\right)\right] \tag{4}$$

$$I(u,v) = \sum_{y=0}^{N-1} \sum_{x=0}^{M-1} f(x,y).\, \sin\left[2\pi\left(\frac{ux}{M} + \frac{vy}{N}\right)\right] \tag{5}$$

As the input image $f(x, y)$ is a real-valued function, the FT of the image exhibits conjugate symmetry. This means that the FT of the image is symmetric with respect to the origin, and the magnitude of the frequency component at a particular position is the same as the magnitude of the corresponding position reflected across the origin. The conjugate symmetry property simplifies the computation of the FT and allows for more efficient algorithms to be used. According to the binary image obtained, in stage 1 and stage 4 in Figure 3, the DFT image lines are extracted.

In stage 1, the lines are energized and appear in the Fourier spectrum with a zero and perpendicular angle. But in the image obtained from the stage 4 because the internal tissue of the battery is damaged, the high and low frequencies in the image are not regular, and in its FT, you can clearly see this change and distinguish a defective battery from a healthy battery.

So, in short, preprocessing the raw image to a binary form and then extracting relevant features it using techniques like DFT are a good starting point that can be improved with hybrid and more complex techniques.

In methods that are based on the analysis of intrinsic features based on the pixels of the image (such as the value of pixels in the histogram method and examination in another space such as the FT), although it can be effective and lead to. These methods can detects failure, but can not perform well in classification and achieving high accuracy in stage identification. To solve this challenge, image classification methods based on neural networks such as CNN can be used. In general, for classifying the level of failure in images, using CNN classification

**Figure 3**
**(a) Fourier transform of part of the internal texture of the battery in step 1 and (b) Fourier transform of part of the internal texture of the battery in step 4**

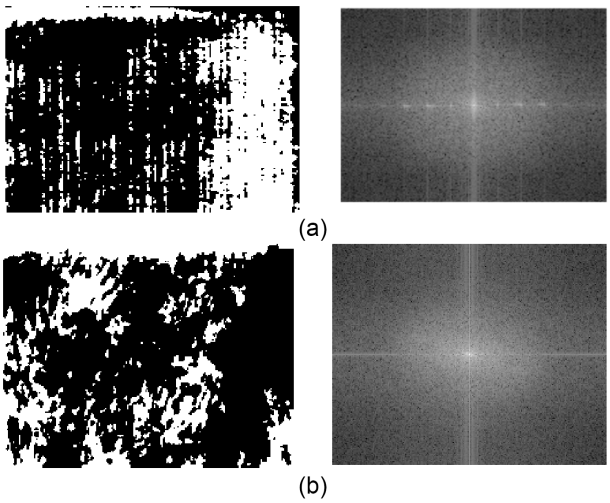


will yield better results compared to binary and DFT image features. CNNs can automatically learn relevant features directly from the input images during training, whereas binary and DFT features require manual, feature engineering. CNNs can learn hierarchical features at different levels of abstraction, allowing them to extract more discriminative information. They are specially designed for image classification tasks, with layers optimized for processing visual data. CNNs can also handle variations in scale of images, pose and lighting and other condition environment better, improving their robustness. When trained on large, labeled datasets, CNNs can achieve very high classification accuracy, outperforming traditional feature-based classifiers. In summary, while binary and DFT features provide some information about failures, CNNs are purpose-built end-to-end models that can learn the most discriminative features directly from images to achieve the best classification performance, provided there is sufficient labeled training data.

## 2.3. Classification of failure stage with improved CNN algorithm

CNNs were first introduced by Hinton and Salakhutdinov (2006) and have since become a popular type of neural network for image classification tasks. One of the key advantages of CNNs over other classifiers is their ability to identify local and higher-level abstract features. In the present study, we designed a CNN network to classify the stages of battery failure.

Our approach involves using convolution layers to extract features from the spatial structure of input images, followed by integration layers to reduce the spatial dimensions of the features. Finally, fully connected layers are utilized to perform the final classification. To train and evaluate our model, we used 60% of the available data for training, 20% for parameter optimization, and 20% for testing. The dataset consisted of four stages of

**Figure 4**
**CNN algorithm used for 4-stage classification of battery images**

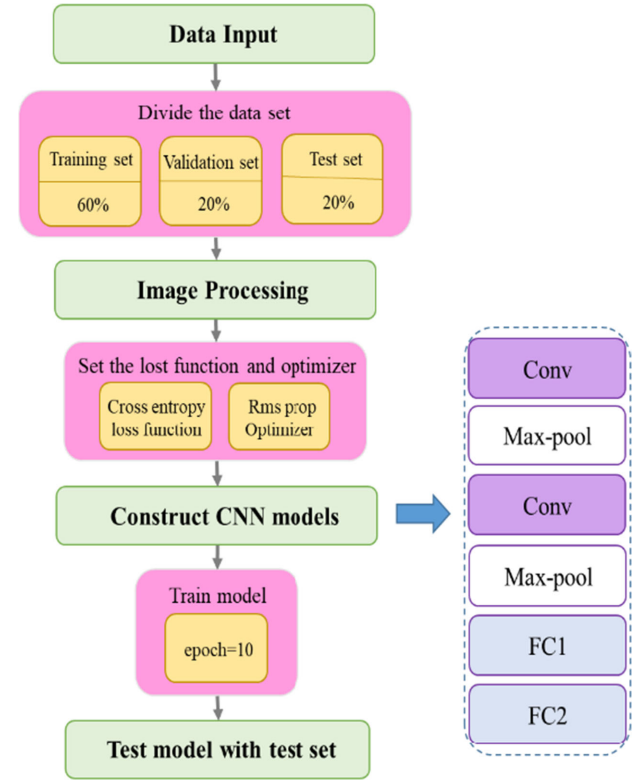


battery failure, and an example of each stage is provided in the accompanying Figure 4.

In our CNN model, we employ 3 × 3 convolutional layers that utilize a set of learnable filters to extract feature maps from the input image. Each filter interacts with the input image to generate a feature map that accentuates specific aspects such as edges, corners, or textures. These feature maps undergo downsizing through 2 × 2 pooling layers, reducing spatial dimensions while preserving essential information. The fully connected layers process the flattened feature maps obtained from the convolutional and pooling layers, culminating in the final classification. We use the modified linear unit (ReLU) as the activation function in each layer, except for the output layer. The output of the fully connected layers is subjected to a softmax activation function, producing a probability distribution across potential classes. Once CNN is trained, it becomes capable of classifying new images. This involves passing these images through the network and using the resulting probability distribution to predict the most probable class. The overall processing flow of our method and the CNN architecture employed for image classification are illustrated in the accompanying figure, divided into four main parts: data division into training, validation, and test sets, preprocessing of original images, training of the constructed CNN model, and finally, testing its performance.

Various techniques have been employed to enhance the performance of CNNs, including data augmentation (van Dyk & Meng, 2001), increasing the number of layers (Nagamura et al., 2020), and modifying the loss function (Pandey et al., 2019), among others. Various techniques exist for enhancing the efficacy of neural networks. One such method involves the incorporation of a kernel into the fundamental framework of these networks. In this study, data augmentation and kernel regularization were utilized to improve the algorithm's performance (Micchelli & Pontil, 2005). This technique helps prevent overfitting by adding a penalty term to the kernel function. The penalty term controls model complexity by discouraging the model from over-relying on a single feature or combination of features. There exist several forms of kernel regularization, such as L1 regularization, L2 regularization, and pure elastic regularization. L1 regularization, also known as lasso regularization, encourages sparse solutions by penalizing the absolute value of the coefficients. In our analysis, we employed L1 regularization with a coefficient of 0.001 for each layer.

In this study, we employ the sparse categorical cross-entropy loss as our chosen loss function. This loss function serves to quantify the dissimilarity between the predicted probability distribution and the true class labels, which are represented as integers. It computes the cross-entropy loss by comparing the predicted probabilities to the actual labels, applying greater penalties to the model for inaccurate predictions that deviate significantly from the true labels. The mathematical formula for the sparse categorical cross-entropy loss is expressed as follows:

$$LOSS = -\frac{1}{N}\sum_{i=1}^{N}\sum_{c=1}^{C}\left(y_{i,c}\ .\ \log(\hat{y}_{i,c})\right) \tag{6}$$

where:

$y_c$ is a binary indicator (0 or 1) of whether class c is the correct classification for the given example.

$\hat{y}_c$ is the predicted probability that the example belongs to class $c$.

$C$ is the total number of classes.

$N$ is the batch size.

To implement data augmentation, considered a rotation range from 0 to 50 degrees, width shift ranges from 0 to 0.2, height shift ranges from 0 to 0.2, and a zoom ranges from 0 to 0.3. Additionally, random horizontal and vertical flips are incorporated, as shown in Figure 5.

**Figure 5**
**Implement data augmentation of battery images**

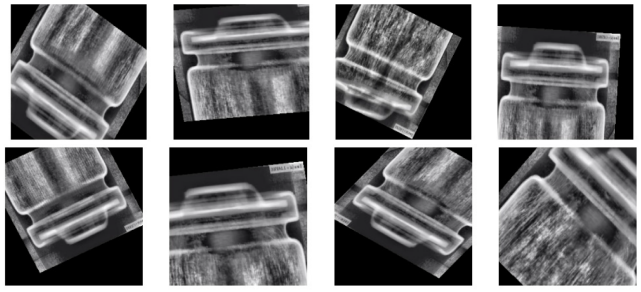

This loss function encourages the predicted probabilities ($\hat{y}_c$) to be close to 1 for the correct class and close to 0 for the incorrect classes. The negative sign is used to turn the minimization problem into a maximization problem (maximizing the log-likelihood of the true class).

Another way to increase the accuracy of CNN is to add transfer learning (TL) to this structure. Weiss et al. (2016) stated that TL is a machine learning technique that involves reusing knowledge acquired from one task to enhance performance on a related task, making it possible to train and fine-tune a classification model using features acquired from other datasets. This is particularly beneficial when data are limited, and training sets lack sufficient images for diverse feature extraction.

To adapt the pretrained model to our specific task, we discard the original classification layers of the pretrained model. These layers are designed for a different classification task and need to be replaced to suit our battery classification problem. Typically, this involves adding one or more fully connected layers followed by an output layer. The output layer has as many neurons as there are battery classes we want to identify. We fine-tune the customized model using our battery image dataset. During training, with trial and error, we adjust hyperparameters such as learning rates, batch sizes, and the number of epochs to optimize the model's performance. After training, we evaluate the model's performance using a validation set. This helps us assess the model's ability to generalize to unseen battery images and make accurate predictions.

One of the famous networks used in TL is DenseNet121. Deep neural network DenseNet121 is a well-known architecture for deep neural networks, which is used for image classification and image processing problems. The most important feature of DenseNet121 is that it uses an idea called "skip connections" or "residual connections" throughout its architecture (Zhou et al., 2022). This idea allows the network to pass information from the lower layers directly to the higher layers, which helps to improve the performance and increase the accuracy of the network. This architecture uses convolutional layers and combinational layers and creates a deep and high-precision network by repeating small blocks.

DenseNet121 consists of a number of convolutions and combinational layers and is used in various applications from object recognition to medical disease diagnosis. This network is known as one of the effective architectures in the field of image processing.

## 3. Results

Incorporating the kernel regularizer into the network structure resulted in a decrease in system speed, but the positive impact on accuracy results, particularly on validation error, was observed and the batch size was 23 with a learning rate of 0.001. Table 3 displays a comparison of the results obtained by applying the kernel regularization technique in the algorithm versus running the algorithm without kernel regularization.

The comparison process and outcomes after 10 epoch are presented in Figure 6, revealing that the CNN's results were achieved despite the limited dataset.

TL was employed, utilizing the pretrained model's parameters as initial values. All layers' parameters were a dropout rate of 0.3 and fine-tuned with a learning rate of 0.001. The corresponding results are presented in Table 4.

Figure 7 shows DenseNet121 had a good convergence rate, and excellent results were achieved despite the limited dataset.

To compare the performance accuracy of the proposed method in Table 5, the results were compared with other TL methods (VGG16, MobileNet121) in 10 epochs. The parameters in all layers were trained at a rate of 0.001 and used the sparse categorical cross-entropy loss function.

Although the results were suitable for other methods as well, the results show that Densenet121 has performed better than other methods.

This set of comparative experiments illustrates that, in the context of data augmentation, kernel regularizer and TL prove to be effective methods for enhancing accuracy. When kernel regularizer is integrated into the network architecture, the outcomes surpass those obtained with a standalone CNN. Through empirical development, a classification model that amalgamated TL with kernel exhibited notably high classification accuracy. Furthermore, the use of TL and data augmentation reduced the reliance on extensive training datasets. Table 6 provides a summary of the results, from initial model selection to subsequent model optimization.

**Table 3**
**Data obtained from CNN algorithm training in 10 epochs**

| epoch | Training loss with kernel | Training loss without kernel | Training accuracy with kernel | Training accuracy without kernel | Validation loss with kernel | Validation loss without kernel | Validation accuracy with kernel | Validation accuracy without kernel |
|---|---|---|---|---|---|---|---|---|
| **1** | **1.5658** | 1.9041 | **0.5296** | 0.5164 | **1.0504** | 1.2517 | 0.2778 | **0.4074** |
| **2** | **0.6398** | 0.7257 | **0.7493** | 0.7096 | **0.5306** | 0.5463 | **0.7037** | 0.6250 |
| **3** | **0.3113** | 0.3423 | **0.8795** | 0.8740 | **0.1326** | 0.3347 | **0.9630** | 0.6991 |
| **4** | 0.2222 | **0.1961** | 0.9151 | **0.9247** | **0.1194** | 0.3847 | **0.9630** | 0.9074 |
| **5** | **0.0646** | 0.1270 | **0.9849** | 0.9493 | 0.2053 | **0.1300** | **0.9683** | 0.9630 |
| **6** | **0.1581** | 0.1010 | 0.9507 | **0.9616** | 0.2095 | **0.0687** | 0.9583 | **0.9722** |
| **7** | 0.1502 | **0.0736** | 0.9507 | **0.9767** | **0.1485** | 0.1882 | 0.9583 | 0.9583 |
| **8** | 0.0734 | **0.0452** | 0.9808 | **0.9863** | **0.0715** | 0.1976 | 0.9583 | 0.9583 |
| **9** | 0.0797 | **0.0580** | 0.9740 | **0.9808** | **0.1152** | 0.1188 | **0.9722** | 0.9630 |
| **10** | 0.0539 | **0.0461** | **0.9890** | 0.9863 | **0.1100** | 0.1529 | **0.9630** | 0.9583 |

**Figure 6**

**(a) Comparison training loss with kernel regularizer and without kernel regularizer, (b) Comparison training accuracy with kernel regularizer and without kernel regularizer, (c) Comparison validation loss with kernel regularizer and without kernel regularizer, and (d) Comparison validation accuracy with kernel regularizer and without kernel regularizer**

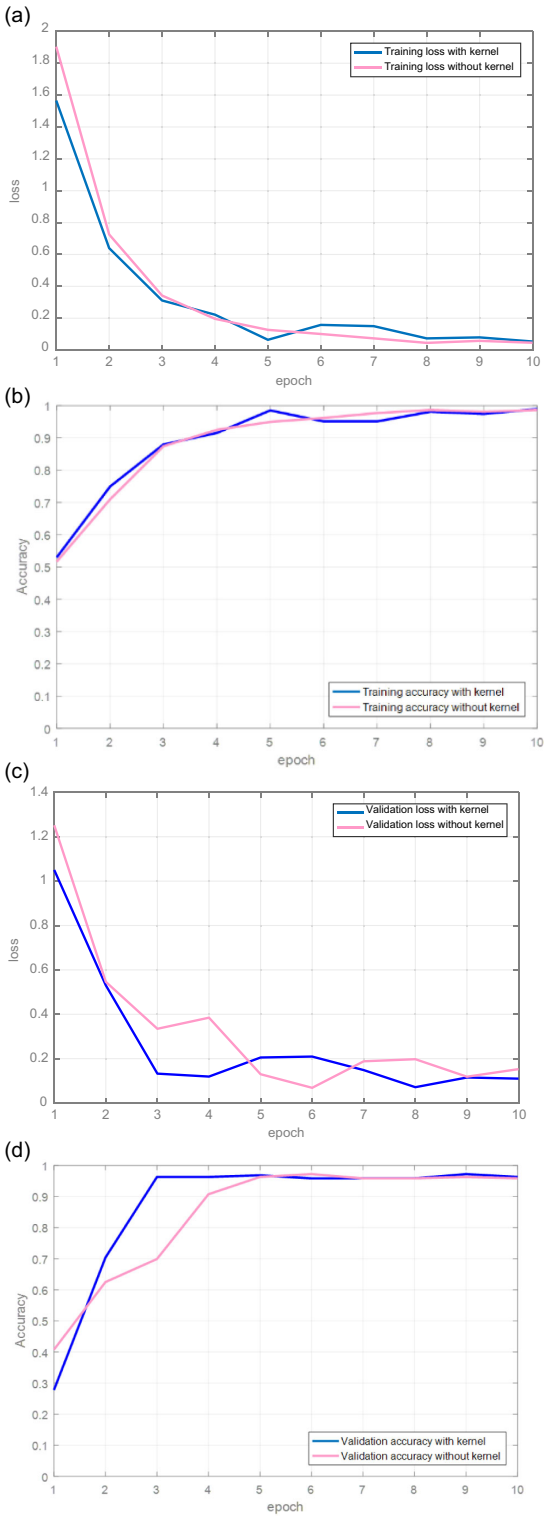


**Figure 7**

**(a) Comparison training loss with kernel regularizer and without kernel regularizer and transfer learning, (b) Comparison training accuracy with kernel regularizer and without kernel regularizer and transfer learning, (c) Comparison validation loss with kernel regularizer and without kernel regularizer and transfer learning, and (d) Comparison validation accuracy with kernel regularizer and without kernel regularizer and transfer learning**

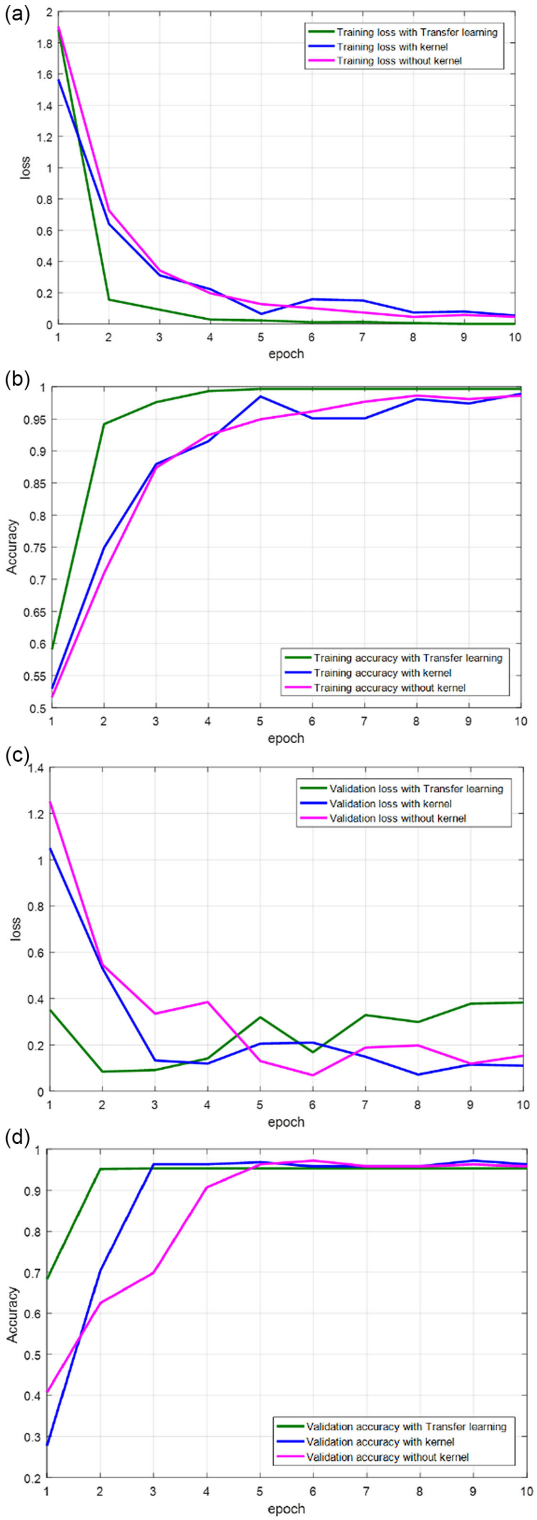

**Table 4**
**Data obtained from DenseNet121 algorithm training in 10 epoch**

| epoch | Training loss with transfer learning | Training accuracy with transfer learning | Validation loss with transfer learning | Validation accuracy with transfer learning |
|---|---|---|---|---|
| **1** | 1.8853 | 0.5908 | 0.3516 | 0.6835 |
| **2** | 0.1556 | 0.9418 | 0.0839 | 0.9520 |
| **3** | 0.0914 | 0.9760 | 0.0911 | 0.9535 |
| **4** | 0.0279 | 0.9932 | 0.1413 | 0.9535 |
| **5** | 0.0226 | 0.9966 | 0.3193 | 0.9535 |
| **6** | 0.0111 | 0.9966 | 0.1681 | 0.9535 |
| **7** | 0.0129 | 0.9966 | 0.3288 | 0.9535 |
| **8** | 0.0058 | 0.9966 | 0.2986 | 0.9535 |
| **9** | 8.5196e-04 | 0.9966 | 0.3781 | 0.9535 |
| **10** | 9.0189e-04 | 0.9966 | 0.3826 | 0.9535 |

**Table 5**
**Results compared to different transfer learning methods based on CNN algorithm training in 10 epoch**

| Model | Training accuracy | Validation accuracy | Test accuracy |
|---|---|---|---|
| DenseNet121 | **0.9966** | **0.9535** | **0.9535** |
| VGG16 | 0.9749 | 0.9475 | 0.8995 |
| MobileNet121 | 0.9802 | 0.9501 | 0.9231 |

**Table 6**
**The results for accuracy in the preferred model**

| Experiment | Training accuracy | Test accuracy |
|---|---|---|
| CNN | 0.9848 | 0.7037 |
| CNN + DA | 0.9863 | 0.8812 |
| CNN + DA + Kernel | 0.9890 | 0.9123 |
| CNN + DA + Kernel + TL | 0.9966 | 0.9535 |

## 4. Conclusion

The aim of this study is to diagnose issues in PV storage systems by analyzing the image characteristics of defective batteries under the influence of thermal runaway. The proposed method successfully distinguishes between normal and inefficient components by examining four stages of battery degradation caused by thermal runaway. The analysis of the obtained images has led to the development of analysis methods that utilize DFT and histogram evaluation for the identification of defective and healthy battery images. Additionally, a classifier based on CNN was proposed to determine the stage of damage. In our experiments, adding a kernel regularizer significantly improved the classification performance in the validation phase, but for the training phase, DenseNet121 was better. Overall, this study presents a promising method for diagnosing problems in PV systems and detecting battery failures caused by thermal runaway. Short circuits within the battery, caused by manufacturing defects, wear and tear, or other factors, can generate excess heat and initiate thermal runaway, and physical damage to a battery, such as punctures, crushing, or short circuits, can disrupt the internal structure and trigger thermal runaway. Future research can include tests on other series. A dataset of batteries can also be based on the analysis of other methods of abuse, including nail penetration, thermal abuse, and internal short-circuiting, and it can also be compared and measured with other algorithms. Also, it is possible to separate the stages more precisely, regarding shorter time intervals and more classes, and increase the accuracy of its calculation. Battery cells with manufacturing defects, including contaminants, internal shorts, or poor quality control, can be prone to thermal runaway. This approach has the potential to serve as a foundation for a new monitoring system and contribute to the development of storage analysis programs in innovative PV systems. These programs can lead to more efficient design, standards, policies, and management of PV structures.

## Acknowledgments

A heartfelt tribute to the resilient Persian women whose lives embody the pursuit of freedom. In the tapestry of our stories, the threads of courage and resilience are woven into a narrative that transcends borders. May the chapters of our lives script a narrative that echoes through generations, inspiring a legacy of liberty and empowerment.

## Conflicts of Interest

The author declares that she has no conflicts of interest to this work.

## Data Availability Statement

The data that support the findings of this study are openly available in National Renewable Energy Laboratory (NREL) at https://www.nrel.gov/transportation/battery-failure.html.

## References

Abbott, M., & Cohen, B. (2020). Issues associated with the possible contribution of battery energy storage in ensuring a stable electricity system. *The Electricity Journal*, *33*(6), 106771. https://doi.org/10.1016/j.tej.2020.106771

Afifah, A. N. N., Indrabayu, Suyuti, A., & Syafaruddin (2020). Hotspot detection in photovoltaic module using Otsu thresholding method. In *2020 IEEE International Conference on Communication, Networks and Satellite*, 408–412. http://doi.org/10.1109/Comnetsat50391.2020.9328987

Amelia, A. R., Irwan, Y. M., Leow, W. Z., Irwanto, M., Safwati, I., & Zhafarina, M. (2016). Investigation of the effect temperature on photovoltaic (PV) panel output performance. *International Journal on Advanced Science, Engineering and Information Technology*, *6*(5), 682–688. http://dx.doi.org/10.18517/ijaseit.6.5.938

Boxwell, M. (2010). *Solar electricity handbook: A simple, practical guide to solar energy-designing and installing photovoltaic solar electric systems*. UK: Greenstream Publishing.

Chen, Y., Kang, Y., Zhao, Y., Wang, L., Liu, J., Li, Y., . . . , & Li, B. (2021). A review of lithium-ion battery safety concerns: The issues, strategies, and testing standards. *Journal of Energy Chemistry*, *59*, 83–99. https://doi.org/10.1016/j.jechem.2020.10.017

Dehghani-Sanij, A. R., Tharumalingam, E., Dusseault, M. B., & Fraser, R. (2019). Study of energy storage systems and environmental challenges of batteries. *Renewable and Sustainable Energy Reviews*, *104*, 192–208. https://doi.org/10.1016/j.rser.2019.01.023

Finegan, D. P., Darcy, E., Keyser, M., Tjaden, B., Heenan, T. M., Jervis, R., . . . , & Shearing, P. R. (2017). Characterising thermal runaway within lithium-ion cells by inducing and monitoring internal short circuits. *Energy & Environmental Science*, *10*(6), 1377–1388. https://doi.org/10.1039/C7EE00385D

Golubkov, A. W., Fuchs, D., Wagner, J., Wiltsche, H., Stangl, C., Fauler, G., . . . , & Hacker, V. (2014). Thermal-runaway experiments on consumer Li-ion batteries with metal-oxide and olivin-type cathodes. *RSC Advances*, *4*(7), 3633–3642. https://doi.org/10.1039/C3RA45748F

Guido, G., Shaffiee Haghshenas, S., Shaffiee Haghshenas, S., Vitale, A., & Astarita, V. (2022). Application of feature selection approaches for prioritizing and evaluating the potential factors for safety management in transportation systems. *Computers*, *11*(10), 145. https://doi.org/10.3390/computers11100145

Hinton, G. E., & Salakhutdinov, R. R. (2006). Reducing the dimensionality of data with neural networks. *Science*, *313*(5786), 504–507. https://doi.org/10.1126/science.1127647

Jung, Y., Oh, H., & Jeong, M. M. (2019). An approach to automated detection of structural failure using chronological image analysis in temporary structures. *International Journal of Construction Management*, *19*(2), 178–185. https://doi.org/10.1080/15623599.2017.1411457

Kamali-Heidari, E., Kamyabi-Gol, A., Heydarzadeh Sohi, M., & Ataie, A. (2018). Electrode materials for lithium ion batteries: A review. *Journal of Ultrafine Grained and Nanostructured Materials*, *51*(1), 1–12. https://doi.org/10.22059/jufgnsm.2018.01.01

Keyser, M., Pesaran, A., Darcy, E., Shoesmith, M., & McCarthy, B. (2015). NREL/NASA internal short-circuit instigator in lithium ion cells. In *Papers Presented at Knowledge Foundation Battery Safety 2013*.

Khatib, T., Ibrahim, I. A., & Mohamed, A. (2016). A review on sizing methodologies of photovoltaic array and storage battery in a standalone photovoltaic system. *Energy Conversion and Management*, *120*, 430–448. https://doi.org/10.1016/j.enconman.2016.05.011

Kim, H. J., Krishna, T. N. V., Zeb, K., Rajangam, V., Gopi, C. V. M., Sambasivam, S., . . . , & Obaidat, I. M. (2020). A comprehensive review of Li-ion battery materials and their recycling techniques. *Electronics*, *9*(7), 1161. https://doi.org/10.3390/electronics9071161

Micchelli, C. A., & Pontil, M. (2005). Learning the kernel function via regularization. *Journal of Machine Learning Research*, *6*(7), 1099–1125.

Mouhib, E., Micheli, L., Almonacid, F. M., & Fernández, E. F. (2022). Overview of the fundamentals and applications of bifacial photovoltaic technology: Agrivoltaics and aquavoltaics. *Energies*, *15*(23), 8777. https://doi.org/10.3390/en15238777

Nabil, A., & Mardaljevic, J. (2006). Useful daylight illuminances: A replacement for daylight factors. *Energy and Buildings*, *38*(7), 905–913. https://doi.org/10.1016/j.enbuild.2006.03.013

Nagamura, Y., Ide, T., Arai, M., & Fukumoto, S. (2020). CNN-based layout segment classification for analysis of layout-induced failures. *IEEE Transactions on Semiconductor Manufacturing*, *33*(4), 597–605. https://doi.org/10.1109/TSM.2020.3029049

National Renewable Energy Laboratory. (2020). *Battery failure databank*. Retrieved from: https://www.nrel.gov/transportation/battery-failure.html

Pandey, R. K., Ramakrishnan, A. G., & Karmakar, S. (2019). Effects of modifying the input features and the loss function on improving emotion classification. In *TENCON 2019-2019 IEEE Region 10 Conference*, 1159–1162. https://doi.org/10.1109/TENCON.2019.8929485

Rahimzadeh, M., Samadi, H., & Shams Mohammadi, N. (2021). Analysis of energy harvesting enhancement in piezoelectric unimorph cantilevers. *Sensors*, *21*(24), 8463. https://doi.org/10.3390/s21248463

Rahimzadeh, M., Samadi, H., & Shams Mohammadi, N. (2023). Improving the efficiency of a cantilever energy scavenger. *Journal of Renewable Energy and Environment*, *10*(1), 59–67. https://doi.org/10.30501/jree.2022.320113.1300

Richardson, D. B., & Harvey, L. D. D. (2015). Strategies for correlating solar PV array production with electricity demand. *Renewable Energy*, *76*, 432–440. https://doi.org/10.1016/j.renene.2014.11.053

Samadi, H., Mohammadi, N. S., Shamoushaki, M., Asadi, Z., & Ganji, D. D. (2022). An analytical investigation and comparison of oscillating systems with nonlinear behavior using AGM and HPM. *Alexandria Engineering Journal*, *61*(11), 8987–8996. https://doi.org/10.1016/j.aej.2022.02.036

Tran, M. K., Mevawalla, A., Aziz, A., Panchal, S., Xie, Y., & Fowler, M. (2022). A review of lithium-ion battery thermal runaway modeling and diagnosis approaches. *Processes*, *10*(6), 1192. https://doi.org/10.3390/pr10061192

Tsai, D. M., Wu, S. C., & Li, W. C. (2012). Defect detection of solar cells in electroluminescence images using Fourier image reconstruction. *Solar Energy Materials and Solar Cells*, *99*, 250–262. https://doi.org/10.1016/j.solmat.2011.12.007

van Dyk, D. A., & Meng, X. L. (2001). The art of data augmentation. *Journal of Computational and Graphical Statistics*, *10*(1), 1–50. https://doi.org/10.1198/10618600152418584

Wang, Y., Zhang, J., Cao, Y., & Wang, Z. (2017). A deep CNN method for underwater image enhancement. In *2017 IEEE International Conference on Image Processing*, 1382–1386. https://doi.org/10.1109/ICIP.2017.8296508

Weiss, K., Khoshgoftaar, T. M., & Wang, D. (2016). A survey of transfer learning. *Journal of Big Data*, *3*(1), 9. https://doi.org/10.1186/s40537-016-0043-6

Xu, B., Lee, J., Kwon, D., Kong, L., & Pecht, M. (2021). Mitigation strategies for Li-ion battery thermal runaway: A review. *Renewable and Sustainable Energy Reviews*, *150*, 111437. https://doi.org/10.1016/j.rser.2021.111437

Zhou, W., Wang, H., & Wan, Z. (2022). Ore image classification based on improved CNN. *Computers and Electrical Engineering*, *99*, 107819. https://doi.org/10.1016/j.compeleceng.2022.107819

**How to Cite:** Shamsmohammadi, N. (2024). Investigating and Classifying the Level of Thermal Runaway-Induced Failure Energy Storage Systems in Photovoltaics. *Journal of Computational and Cognitive Engineering*, *3*(1), 15–23. https://doi.org/10.47852/bonviewJCCE32021698